Influence of instability modes on cooling performance in hypersonic boundary layer with slot injection

CERMINARA, Adriano, HERMANN, Tobias <http://orcid.org/0000-0002-6253-6068>, IFTI, Hassan Saad <http://orcid.org/0000-0002-8398-8987>, DEITERDING, Ralf, SANDHAM, Neil and MCGILVRAY, Matthew

Citation:

Copyright and re-use policy

Influence of instability modes on cooling performance in hypersonic boundary layer with slot injection

Adriano Cerminara[a,1,*], Tobias Hermann[b], Hassan Saad Ifti[b], Ralf Deiterding[a], Neil Sandham[a], Matthew McGilvray[b]

[a]*Aerodynamic and Flight mechanics Research Group, University of Southampton, Southampton, Hampshire, SO17 1BJ, United Kingdom*
[b]*Oxford Thermofluids Institute, University of Oxford, Oxford, Oxfordshire, OX2 0ES, United Kingdom*

Abstract

A combined numerical-experimental investigation is presented with focus on the effects of boundary-layer instabilities and transition on the wall cooling performance in a Mach 5 low-enthalpy flow over a flat plate, with coolant injection achieved through a row of slots. The numerical study has been performed through direct numerical simulation (DNS) of the compressible Navier-Stokes equations, and is supported by results from linear stability analysis (LST) for the considered boundary layer. The experiments have been conducted in the High Density Tunnel (HDT) of the Oxford Thermofluids Institute, and includes several blowing ratio conditions of injected air for the same freestream conditions. Surface heat transfer and pressure measurements, film effectiveness measurements, and Schlieren images are presented. The analysis links the wall cooling performance to the growth of imposed unstable boundary layer modes. Results indicate that 2D and 3D unstable modes, pertaining to the class of first instability modes, exist in the laminar boundary layer, and that imposition of these modes at different amplitudes leads to different states of the boundary layer, which we refer to as a perturbed state and a transitional state for medium and high amplitude respectively. As confirmed by comparison with experimental

---

[*]Corresponding author
   Email address: `a.cerminara@wlv.ac.uk` (Adriano Cerminara)
   [1]Faculty of Science and Engineering, Telford Innovation Campus, University of Wolverhampton, Telford TF2 9NT, UK

data, the perturbed and transitional states of the boundary layer significantly affect the wall cooling performance, providing an increase of the wall heat flux that results in a reduction of the beneficial effects of cooling.

1. Introduction

In hypersonic flows, where aerodynamic heating compromises the vehicle structure integrity, the film cooling technique [1, 2] represents a valid solution to suppress the heat loads experienced by the surface material. This technique is aimed at injecting coolant into the hot boundary layer to form a thin film of cold fluid adjacent to the wall, thus reducing the wall heat flux. Two different injection strategies can be distinguished, namely effusion cooling [3, 4], and transpiration cooling [5, 6]. The former provides injection through localised holes, and is typically used for thermal protection of turbine blade surfaces, in which cooling occurs through a turbulent mixing layer. The latter, in contrast, takes advantage of the transpiration capabilities of a porous material to provide a more uniformly distributed coolant film. In a supersonic-hypersonic flow, however, the wall cooling requirement is combined with the requirement of increasing the laminar run of the boundary layer, i.e. delaying transition. For this reason, injection through two-dimensional slots may be preferred, as it reduces the 3D effects associated with hole injection [7, 8, 9].

Besides film cooling, efforts have been made in the past decade to achieve hypersonic boundary-layer stabilisation through the use of porous coatings [10, 11]. This technique uses the acoustic absorption capabilities of porous materials to suppress or damp the second instability mode, which is known to be the dominant mode in 2D hypersonic boundary layers [12]. Several numerical [13, 14] and experimental [15, 16, 17] studies have been conducted to validate this methodology and to investigate the main parameter dependence for the reduction of the second mode growth rate, and more recent studies have focused on the characterisation and modeling of the acoustic absorption properties of carbon-carbon

2

(C-C) type porous ceramic materials, identified as optimal candidates for the second-mode attenuation [18, 19] in thermal protection systems.

The objective of our study is to consider, from a fundamental perspective, both wall cooling and boundary-layer stability properties simultaneously, which can potentially lead to the design of novel porous materials for new-generation transpiration-cooling-based thermal protection systems that combine both the capability of injecting coolant fluid through the pores and of stabilising the boundary layer. As a first step to such investigation, the focus here is on the effects that the evolution of the dominant unstable boundary-layer modes, induced by locally imposed perturbations, have on the wall cooling capabilities, in comparison with an ideal case without disturbances and a case in which transition to turbulence is triggered by high-amplitude disturbances. Furthermore, this study is motivated by the fact that, in the real experimental conditions of conventional hypersonic wind tunnels, the boundary layer on the probe is known to be perturbed by different sources of noise, coming e.g. from the turbulent boundary layer at the nozzle walls, or from vorticity waves or entropy spottiness coming directly from the upstream reservoir. The acoustic noise radiated from the turbulent boundary layer on the nozzle walls, in particular, is known to be the dominant source of disturbances inside conventional hypersonic wind tunnels [20, 21, 22]. Moreover, other types of uncontrolled factors, e.g. small undetected rougness elements or geometrical discontinuities on the model surface, can introduce additional disturbances that affect the state of the boundary layer, e.g. by enhancing the growth rate of the instabilities or exciting other instability modes, thus affecting the transition mechanism.

In the present work, disturbances inside the boundary layer are simulated by imposing an unsteady blowing-suction model to excite the dominant instability modes. The choice of the amplitude is based on the findings of recent experimental as well as numerical studies [23, 24, 25, 26], aimed at investigating the noise characteristics in the environment of hypersonic wind tunnels. The comparison between the theoretical results of a linear stability study, the numerical results from the DNS, and the experimental data provides an indication of the

3

influence of the unstable mode evolution and initiation of the transition process on the cooling performance for a hypersonic flow over a flat plate with slot injection, as well as information about how this effect depends on the blowing ratio and on the amplitude level of the disturbances.

2. Numerical method

2.1. Governing equations

The system of the three-dimensional dimensionless governing equations for compressible multispecies flows, written in conservation form, under the assumption of constant specific heats, is given in Cartesian coordinates as

$$\frac{\partial \rho}{\partial t} + \frac{\partial \rho u_j}{\partial x_j} = 0 \ , \tag{1}$$

$$\frac{\partial \rho u_i}{\partial t} + \frac{\partial \rho u_i u_j}{\partial x_j} = -\frac{\partial p}{\partial x_i} + \frac{1}{\mathrm{Re}} \frac{\partial \tau_{ij}}{\partial x_j} \ , \tag{2}$$

$$\frac{\partial \rho E}{\partial t} + \frac{\partial \left(\rho E + \frac{p}{\rho} \right) u_j}{\partial x_j} = \frac{1}{(\gamma - 1)\mathrm{RePr}M^2} \frac{\partial}{\partial x_j} \left(\kappa \frac{\partial T}{\partial x_j} \right)$$
$$+ \frac{1}{\gamma \mathrm{ReSc}M^2} \frac{\partial}{\partial x_j} \left(\rho D \sum_k \frac{\partial c_k}{\partial x_j} c_{p,k} T \right) + \frac{1}{\mathrm{Re}} \frac{\partial \tau_{ij} u_i}{\partial x_j} \ , \tag{3}$$

$$\frac{\partial \rho c_k}{\partial t} + \frac{\partial}{\partial x_j} \left(\rho c_k u_j - \rho D \frac{\partial c_k}{\partial x_j} \right) = 0 \ . \tag{4}$$

The terms ρ, ρu, ρv, ρw and ρE are the conservative variables of the system of equations, where ρ is the density, u, v and w are the velocity components respectively in the x-, y- and z-directions, E is the total energy per unit mass, and the terms p, T, τ_{ij}, and μ are respectively the pressure, temperature, viscous stress tensor components and dynamic viscosity. The physical variables are normalised through their freestream reference values, except for the pressure, which is normalised with the term $\rho_\infty^* U_\infty^{*2}$, and the energy, which is normalised with U_∞^{*2}. The superscript $(^*)$ is used to denote dimensional values. The characteristic length is taken as the boundary-layer displacement thickness (δ^*) of

4

the similarity solution at the inflow. The characteristic fluid dynamic time is δ^*/U_∞^*. The terms Re, Pr, Sc, M, and γ are respectively the Reynolds, Prandtl, Schmidt and Mach numbers, and the ratio of specific heats, $\gamma = c_{p,\infty}^*/c_{v,\infty}^*$, in the freestream, i.e. the dimensionless parameters of the flow. The Reynolds number is defined as Re $= (\rho_\infty^* U_\infty^* \delta^*)/\mu_\infty^*$; the Prandtl number is set to 0.72, and γ is equal to 1.4, as the freestream gas is air. The Schmidt number is defined in terms of the mass diffusivity as Sc $= \mu_\infty^*/(\rho_\infty^* D_\infty^*)$. Wilke's rule is used to express the dynamic viscosity of the mixture, as described in [27], and a power law is used to evaluate the single species viscosity. The thermal conductivity is then expressed in terms of the species viscosity, Prandtl number, specific heat and mole fraction through the following formula,

$$\kappa = \sum_k \left(\frac{X_k \frac{\mu_k c_{p,k}}{\text{Pr}_k}}{\sum_l X_l \phi_{kl}} \right) , \tag{5}$$

with the term ϕ_{kl} defined as in [27]. All the transport properties used in the present work are relative to a binary mixture and can be found in [8, 27, 28]. The system of the governing equations is closed by the relation for the total energy,

$$E = \frac{1}{\gamma M^2} c_v T + \frac{1}{2} \left(u^2 + v^2 + w^2 \right) , \tag{6}$$

and by the equation of state,

$$p = \frac{1}{\gamma \text{M}^2} \rho R T . \tag{7}$$

The specific heats at constant volume and pressure, namely c_v and c_p respectively, as well as the gas constant R, represent mixture properties, which are given as [8]

$$c_v = c_1 c_{v,1} + c_2 c_{v,2} , \tag{8}$$

$$c_p = c_1 c_{p,1} + c_2 c_{p,2} , \tag{9}$$

5

and

$$R = c_p - c_v \; . \tag{10}$$

It should be mentioned that the normalisation factor for the mixture gas constant and specific heats is the freestream reference value, i.e. the air gas constant, $R_\infty^* = 287.058$ J/(Kg K).

2.2. Numerical scheme

The finite-volume method used to solve numerically the governing equations consists of a 6th-order central differencing (CD) scheme in space for both inviscid and viscous fluxes, combined with a 6th-order weighted-essentially-non-oscillatory (WENO) scheme for shock capturing, along with a 3rd-order Runge-Kutta method for time integration. The so-called WENO-CD scheme is provided with a switch function that turns on/off the shock-capturing scheme at discontinuities and in smooth flow regions, respectively, and has been validated over the past years for several types of compressible high speed flow configurations [29, 30, 31, 32, 33, 34].

The code is also provided with a structured adaptive mesh refinement (SAMR) method, which enables high-resolution in the small length scales of the pore region. This technique, decribed in [35], allows consecutive higher grid refinement levels to be dynamically added in the high-gradient flow regions in a patch-wise fashion, thus providing higher numerical stability and solution accuracy in the flowfield as well as minimising the computational cost.

3. Linear stability analysis

The linear stability analysis was performed using the NoSTRANA (Nonlocal Stability and Transitional Analysis) code by Sansica [36]. The code solves the linearized Navier-Stokes equations, based on a normal mode ansatz

$$\mathbf{q}'(x, y, z, t) = \hat{\mathbf{q}}(y) \cdot e^{(i(\alpha x + \beta z - \omega t))} \; , \tag{11}$$

in which α represents the streamwise wavenumber, β the spanwise wavenumber, and ω the angular frequency of the periodic wave perturbation. The linear

system of partial differential equations reduces to a linear system of ordinary differential equations in the variable y, which can be expressed as

$$\mathbf{L}\hat{\mathbf{q}} = \omega \mathbf{K}\hat{\mathbf{q}} \ , \tag{12}$$

where $\mathbf{L}$ is a matrix containing the y-dependent coefficients of the system, the wavenumbers α, β, and the y-derivatives of the components of the variable vector $\hat{\mathbf{q}}$; while $\mathbf{K}$ is a diagonal matrix containing the terms multiplied by ω, which come out from the time derivatives of equation (11). The system defined in (12) represents an eigenvalue problem. The resolution of this eigenvalue problem, at a particular x-location along the wall provides a certain number of eigenvalues and corresponding eigenvectors $\hat{\mathbf{q}}(y)$, containing the eigenfunctions $\hat{\rho}(y)$, $\hat{u}(y)$, $\hat{v}(y)$, $\hat{w}(y)$, $\hat{T}(y)$, representing, in turn, the shape of each mode inside the boundary layer at that particular x location. The discretisation of the system in the wall-normal direction is made through a Chebyshev collocation method. Sansica [36] derives all the components of the matrices $\mathbf{L}$ and $\mathbf{K}$ in (12), and gives a description of the Chebyshev discretisation method. The present work focuses on results from the temporal formulation, in which real values for the streamwise and spanwise wavenumbers are imposed and the eigenvalues ω are computed. The real part (ω_r) represents the angular frequency, while the imaginary part (ω_i) represents the temporal growth rate. Temporal growth rates can be easily transformed into spatial growth rates using Gaster's relation [37]

$$\frac{\omega_i}{\alpha_i} = -\frac{\partial \omega_r}{\partial \alpha_r} = -c_g \ , \tag{13}$$

which is exact for neutral modes and accurate for weak growth rates of the kind seen in the present study. In the present work the linear analysis is performed at several x stations along the plate, and for different streamwise wavenumbers (α).

95 4. Experimental setup

The experiments are conducted in the High Density Tunnel (HDT) of the Oxford Thermofluids Institute [38], operating as a heated Ludwieg tunnel. It

7

consists of a 17.4 m long barrel with an internal diameter of 152.4 mm which is filled with high pressure air before each experiment. A bespoke fast-acting plug valve separates the barrel from a contoured nozzle and the facility test section. Steady state test times achieved in the facility last for approximately 40 ms.
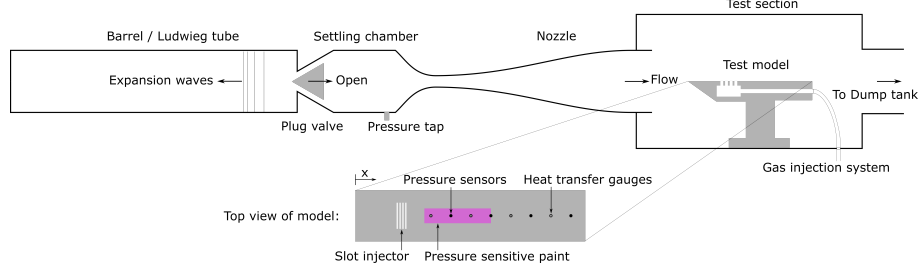

Figure 1: Sketch of HDT with the installed flat plate test model

The test model mounted in the wind tunnel is shown schematically in figure 1 and is 580 mm long and 125 mm wide. An insert with a series of four slots is used to inject gas into the boundary layer, where each of the slots is 0.2 mm wide (in the streamwise direction), 30 mm long (in the spanwise direction), with a depth of 1.5 mm, and separated from one another by a distance of 1 mm. The first slot is located 177 mm from the model tip. The injected coolant gas is Air.

The injected mass flow rate has been calibrated with respect to the measured plenum pressure in a post test analysis. The free stream and injection conditions are given in table 1.

The operational range of the slot injector includes a condition of no injection, which is referred to as condition A, and four different injection conditions at increasing plenum pressure. These injection conditions, taking as reference the freestream pressure p_∞ and neglecting the 'plenum' subscript, can be listed as: B) $p_0^* = 1.6 p_\infty^*$, $F = 0.045$, C) $p_0^* = 1.8 p_\infty^*$, $F = 0.066$, D) $p_0^* = 2.7 p_\infty^*$, $F = 0.11$, and E) $p_0^* = 4.8 p_\infty^*$, $F = 0.23$. In the given conditions, F denotes the blowing ratio as defined in table 1. The surface of the model downstream of the injector is instrumented with three Kulite XCEL-152-25A pressure transducers, and four platinum thin film gauges on quartz bodies that provide temperature readings from voltage variations [39]. Both sensor types are located on the centreline of

8

Table 1: Flow conditions run for this study

Coolant gas	Air
Angle of attack / deg	0
M	5
p^*_{fill} / kPa	1623
T^*_{fill} / K	537
[1]$Re_{x,\text{injector}}$	$2.24 \cdot 10^6$
$p^*_{0\infty}$ / kPa	864
[2]$T^*_{0\infty}$ / K	460
[3]$p^*_{0,plenum}$ / kPa	$2.6 - 8.7$
[4]p^*_s / kPa	1.74
$F = (\rho^*_{inj} v^*_{inj})/(\rho^*_\infty u^*_\infty)$	$0.045 - 0.23$

[1] Reynolds based on the distance of the injector location from the leading edge.

[2] Measurement by aspirated thermocouples.

[3] Measurement by plenum pressure sensor.

[4] Measurement by static pressure sensor on plate surface.

the model. The experimentally recorded temperature data is used to calculate the surface heat flux by applying the impulse response convolution approach of Oldfield [40]. Further details on the intrumentation and the HDT run conditions can be found in [41].

₁₂₅ The heat-flux sensor considered in the numerical simulations corresponds to the first film gauge, and is located at a distance of 247 mm from the plate leading edge and 70 mm from the slot injector. The slot size in the spanwise direction was designed to be sufficiently higher than the x-wise size (with an aspect ratio of $l_z/l_x = 150$) to provide minimum 3D flow effects from the slot edges up to

₁₃₀ relatively high distances downstream of the injection location. By denoting the dimensional distance from the plate leading edge as x^*_{LE}, based on the Mach angle corresponding to the $M = 5$ flow condition, the effect of the plate edges would reach the centreline for $x^*_{LE} \geq 307$ mm, whereas the effects associated to the edges of the slots should reach the centreline for $x^*_{LE} \geq 251$ mm. Thus,

9

although it is not possible in general to exclude the presence of 3D effects in the experiments, these estimations allow us to perform numerical simulations on a relatively narrow domain in the z-direction centred on the centreline, assuming spanwise periodicity, as will be described in Section 5.

5. Problem specification for the simulations

5.1. Domain and boundary conditions

As sketched in figure 2, coolant is injected into the boundary layer through four equally-spaced span-periodic slots, which are fed underneath by a plenum chamber. The plenum boundary conditions are imposed at the bottom boundary as stagnation pressure (p_0) and stagnation temperature (T_0).

The freestream conditions correspond to $M = 5$, Re = 12600, $T_\infty^* = 76.6$ K, and the wall temperature is fixed to the room temperature, $T_w^* = 290$ K. The flow is initialised with the laminar boundary layer from the similarity solution, with an inflow displacement thickness of $\delta_0^* = 1$ mm. The inlet of the computational domain is at a distance of 127 mm from the plate leading edge, and the first slot is placed at a distance of 50 mm from the inlet, corresponding to a distance of 177 mm from the plate leading edge. The dimensional value of the inflow boundary-layer displacement thickness of the similarity solution corresponds to a thickness of about $\delta_{99}^* = 1.25$ mm, which is a good estimation of the boundary-layer thickness in the real experiment at the inflow location (127 mm from the plate leading edge) from Van Driest's empirical correlations [27] for the considered Mach number.

The domain dimensions are $L_x^* = 160$ mm, $L_y^* = 32$ mm, $L_z^* = 8$ mm. The four slots have the same dimensions in the x- and y- directions as described in Section 4, and span the full domain width in the z- direction with periodic boundaries. The grid size is $N_x \times N_y \times N_z = 3200 \times 384 \times 40$. The domain width (8 mm) was chosen according to the LST results presented in Section 6, whereas the grid size in the spanwise direction was chosen according to the

10

domain width, and consistent, as the grid size in the other directions, with a grid study described in [42].
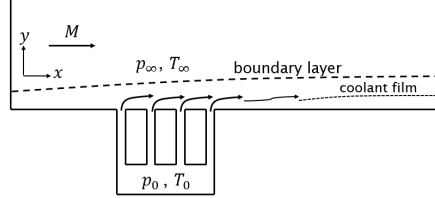

Figure 2: Sketch of coolant injection

5.2. Validation test case against other numerical and experimental results

A similar problem of laminar film cooling in a Mach 2.6 flow through a single slot has been considered as a test case for code validation, in which results were compared against numerical and experimental results available in the work of Keller et al. [8].

170   Results of the validation study for the case of CO_2 injection are reported. shown in figure 3, in which the cooling effectiveness distribution downstream of the injection location is plotted against a normalised distance. As in Keller et al. [8], the cooling effectiveness has been computed using the following formula

$$\eta = 1 - \frac{q_{w,c}}{q_{w,nc}} \ , \tag{14}$$

in which $q_{w,c}$ represents the computed heat flux in the case with cooling, and
175    $q_{w,nc}$ is the heat flux without cooling. As can be seen, our numerical results agree very well with both computational and experimental results reported in [8], thus verifying the capabilities of our numerical scheme to achieve accurate results for the general case of film cooling in a binary mixture in a compressible boundary layer. Similar results were obtained also for the case of air injection.
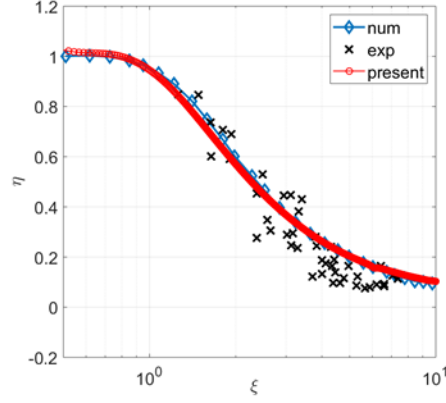
11

Figure 3: Cooling effectiveness for CO_2 injection

6. Results

Figure 4 shows a qualitative comparison based on a Schlieren image at the slot injector between the numerical and experimental results. It should be noted that the experimental Schlieren integrates across the span of the test plate. The two images show important similarities about the main flow features of injection in a hypersonic boundary layer. The boundary layer gets gradually thicker up to the injector location, with a comparable gradient $(\partial \delta(x)/\partial x)$ between numerical and experimental results, then a more pronounced increase in thickness is observed at the injection location, followed by a slight reduction further downstream. At the bump location, the formation of the forefront shock wave is visible, followed by an expansion fan (the whiter region developing upwards) and by a second shock originating at the end of the bump, in the concave region that produces the downstream reduction of the thickness.
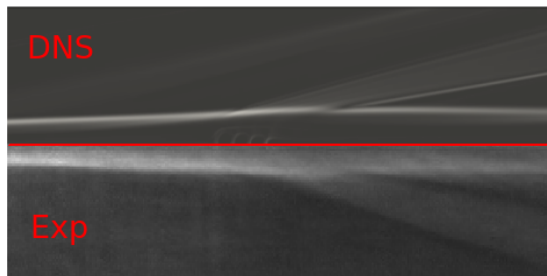
12

Figure 4: Schlieren image comparison between DNS results (top) and experimental results (bottom)

In order to carry out a systematic study of the effect of unstable distur-
bances, at different initial amplitudes, on the wall-cooling performance, local
linear stability analysis was used to identify the most unstable modes at the
heat-flux sensor location, i.e. $x = 120$. This allows to associate the behaviour
related to the wall cooling performance at the sensor location with the growth of
the unstable modes in the upstream region. After having identified the unstable
modes in the laminar unperturbed (baseflow) boundary layer, these are intro-
duced upstream of the injection slots by a 3D blowing-suction model applied on
the wall.

The results of the LST study are shown in figure 5 for the temporal growth
rates and frequencies of 2D modes respectively, and plotted against the mode
streamwise wavelength (λ^*). As can be seen, the region of instability involves
2D modes with a wavelength higher than about 10 mm and frequencies be-
low 50 kHz, with the most unstable mode being characterised by a streamwise
wavelength of approximately 31 mm (corresponding to the peak location of the
ω_i curve in figure 5). These modes pertain to the class of the first instabili-
ties. By performing a linear stability analysis involving also non-zero spanwise
wavenumbers, it is found that the most unstable first mode is a 3D mode with
wavenubers $\alpha = 0.2$, and $\beta = 0.78$, corresponding to a wavelength of 31 mm in
the streamwise direction, and a wavelength of 8 mm in the spanwise direction,
and with frequency $f^* = 12.5$ kHz. The temporal growth rate associated with
this mode is $\omega_i = 4.29 \times 10^{-3}$. Hence, from LST analysis it is found that the

13

baseflow is unstable to 2D and 3D modes corresponding to the class of first instability modes up to the heat-flux sensor location. The higher frequency modes (above 100 kHz) observed in figure 5 pertain, instead, to the class of the second instability modes, however they are not found to be unstable at this location. They are then expected to get unstable and to represent the dominant instability further downstream and outside of our computational domain.
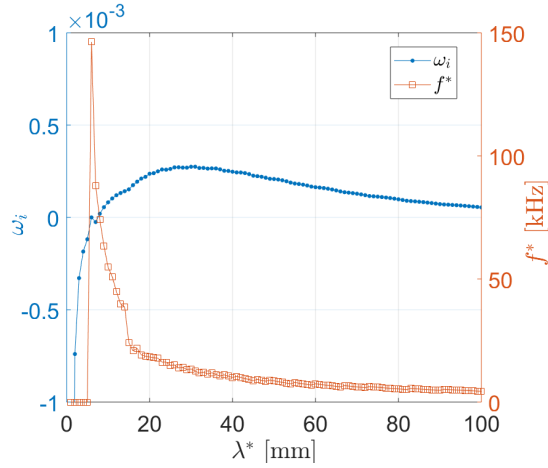

Figure 5: Temporal growth rates and frequencies of the unstable 2D modes from LST

After having found the dominant instabilities that can grow and interact with the coolant gas, these modes are now introduced at an upstream location in order to perturb the boundary layer and observe the sensitivity of the cooling performance to the growth of the perturbations. This is achieved by imposing a blowing-suction model for the vertical velocity on the wall, at the streamwise location $x = 20$, as follows

$$v'(x, z, t) = \sum_{m=1}^{M} \left(A \cos\left(\beta_m z + \phi_m\right) \cos\left[\alpha(x - x_0) - \omega t + \psi\right] \right), \qquad (15)$$

where m is the integer number representing the spanwise wave mode, M is the total number of oblique waves, A is the disturbance amplitude, ω is the angular frequency, and the phase angles are set as $\phi_m = \psi = 0$. The streamwise and spanwise wavenumber as well as the frequency of the most unstable 2D and 3D

14

modes are imposed through this model. Two different amplitudes have been considered, namely $A = 5 \times 10^{-3}$ and $A = 2 \times 10^{-2}$, to simulate moderate and strong perturbations.
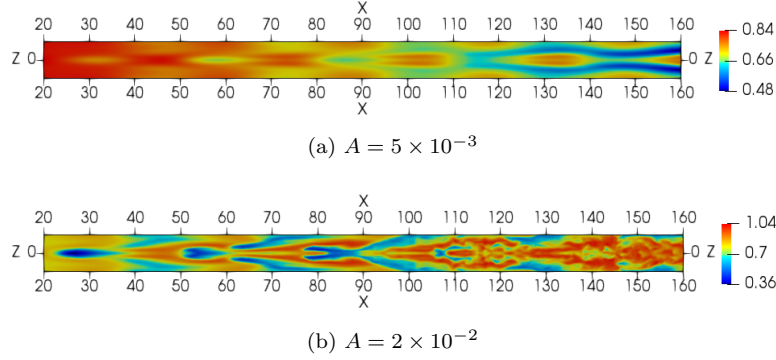

(a) $A = 5 \times 10^{-3}$

(b) $A = 2 \times 10^{-2}$

Figure 6: Streamwise velocity u at $y = 1$ inside the boundary layer

Figure 6 shows contours for the streamwise velocity (u) inside the boundary layer at the height $y = 1$. The flow structure reveals the imprint of the oblique first mode growth in the streamwise direction. At the lower amplitude, a gradual growth is observed, with the appearance of streaks in the downstream region, whereas breakdown has started to occur at the higher amplitude, with evidence of the formation of smaller scales.

The corresponding time-averaged skin friction coefficient profiles downstream of the slot injector location are shown in figure 7. In the moderate amplitude case, the skin friction shows a rapid growth in the downstream region, indicating a perturbed state of the boundary layer which precedes transition. In the high amplitude case, the skin friction assumes much higher values, consistent with the state of a breakdown to turbulence.
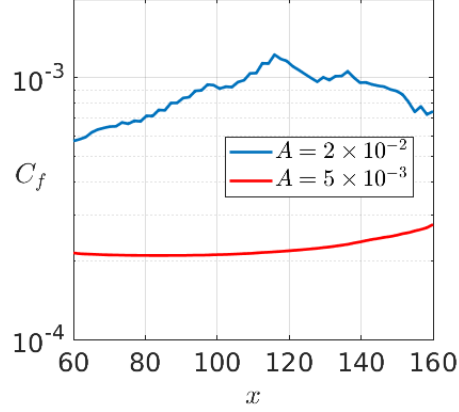
Figure 7: Time-averaged skin friction coefficient

Figure 8 shows results for the streamwise velocity cross-sections in the yz-plane at the heat-flux sensor location (x=120) for the case without injection (case A), and the case with highest injection rate (case E), at both disturbance amplitudes. The flow structures in condition A show a laminar perturbed boundary layer at the lower amplitude, and a transitional boundary layer at the higher amplitude. A similar behaviour is obtained for the other injection cases from B to D. For the strong injection case (condition E), instead, it is observed that transition is reached for both amplitudes. However, while the flow patterns at the higher amplitude are similar to those observed in the corresponding case of condition A, at the lower amplitude the transition patterns are different. This is due to the fact that in the higher amplitude case the main source of the transition mechanism is the high disturbance amplitude, whereas in the lower amplitude case, transition is induced by the strong blowing.
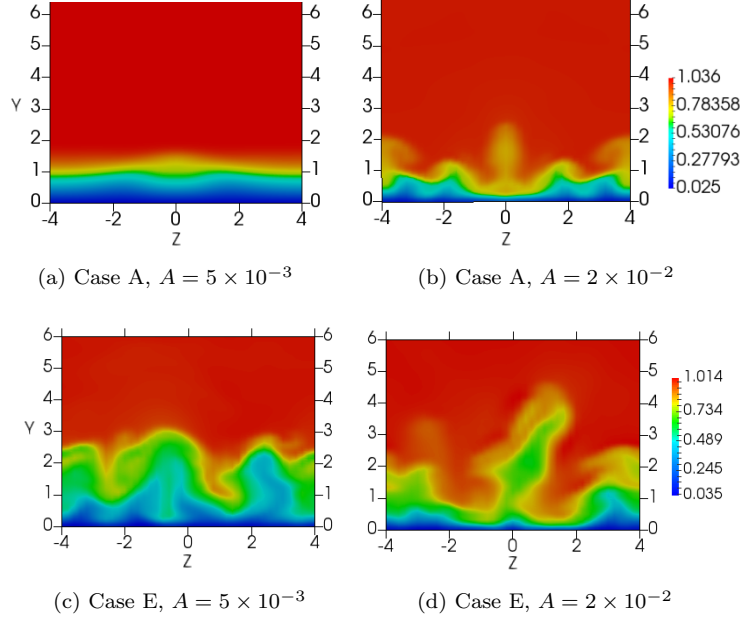
16

(a) Case A, $A = 5 \times 10^{-3}$ (b) Case A, $A = 2 \times 10^{-2}$

(c) Case E, $A = 5 \times 10^{-3}$ (d) Case E, $A = 2 \times 10^{-2}$

Figure 8: Streamwise velocity u cross-section in a yz-plane at $x = 120$

After having classified the different states of the boundary layer, attention
is now given to understanding the effect of these different states on the cooling
performance at the different plenum pressures, and compare the results with the
experimental measurements. Figure 9 show the coolant mass fraction contours
inside the boundary layer for cases C and E. Case C at the low amplitude is
representative also of cases B and D. Here, two important observations can be
made. First, in the laminar case (lower injection and low wave amplitude) a
particular pattern of the coolant distribution is observed, following the structure
of the first oblique mode evolution (seen in figure 6a). In particular, the coolant
appears to concentrate along the low-speed streaks in figure 6a. Furthermore, a
noticeable difference is observed in case E (strong blowing) between the low and
high amplitude cases, which is due to the difference in the transition mechanism.
In the high-blowing transitional case (figure 9b), the coolant is seen to persist up
to longer distances downstream. In the high-disturbance case, in contrast, the
coolant is seen to disappear rapidly downstream. The cause of this appears to

17

be the mushroom-like structure forming at the mid-span location ($z = 0$) with two counter-rotating vortices at the sides characterising the high amplitude case (see figure 6d). This flow pattern causes the low-speed coolant-rich near-wall fluid to be transported from the wall to the upper layers, and vice-versa.

(a) Condition C, $A = 5 \times 10^{-3}$

(b) Condition E, $A = 5 \times 10^{-3}$

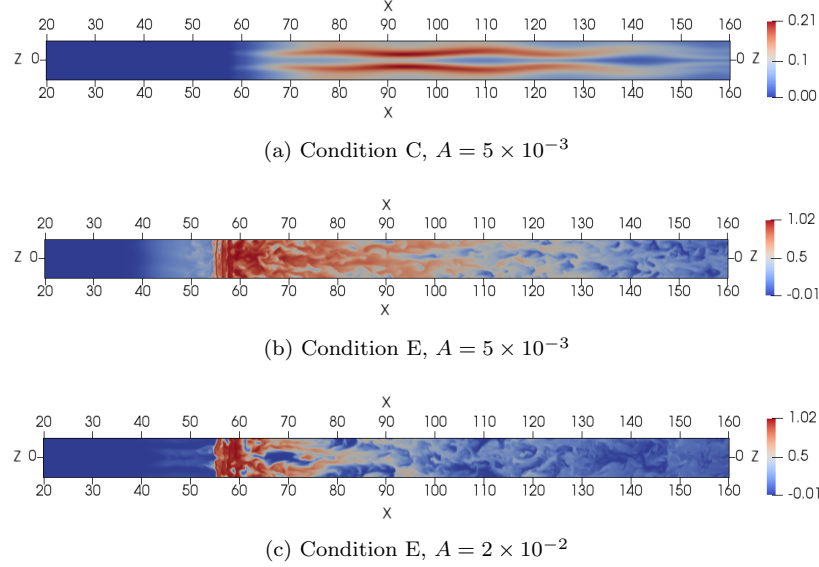(c) Condition E, $A = 2 \times 10^{-2}$

Figure 9: Coolant mass fraction distribution at $y = 1$ inside the boundary layer

The effect of the above-described features on the cooling performance in comparison with the real experimental cases can be seen in figure 10, which shows results for the wall heat flux at the sensor location for the different blowing ratios. The numerical results are presented for the cases of no disturbances, moderate 2D disturbances, moderate 3D disturbances, and high 3D disturbances. As can be seen, when considering simulations without disturbances (the ideal laminar state), the heat flux rapidly decreases as the plenum pressure is increased, diverging from the experimental values. Whereas, when considering the presence of the most unstable modes (2D and 3D) at a moderate amplitude, a reasonably good agreement with the measurements is achieved, thus indicating that in realistic conditions the boundary layer is in a perturbed state, for the case with blowing. In the case without blowing, in contrast, the experimental results

18

are in a better agreement with those of the simulation without disturbances. This, in turn, would suggest that the presence of blowing has the effect of enhancing the growth of initial disturbances such that simulations with imposed perturbations are more representative of a real case, whereas without blowing disturbances would maintain a smaller amplitude at the considered streamwise location, hence such a condition is better represented by an ideal (i.e. no disturbance) simulation. When considering high disturbance amplitudes, instead, the obtained heat-flux values are significantly higher than the experimental values, which is due to the flow rapidly going through transition to turbulence in this case.

A further confirmation of the agreement between numerical and experimental results in terms of the cooling performance is provided in figure 11, which shows results of the cooling effectiveness downstream of the slot injector. Note that the film effectiveness in figure 11 has been computed based on the coolant concentration, through the following formula [41, 43],

$$\eta = \frac{C_w - C_e}{C_c - C_e}, \tag{16}$$

where C represents the oxygen mass fraction either at the wall (w), at the boundary layer edge (e), or within the coolant (c).

As can be seen in figure 11, the effectiveness is decreasing with the distance from the slot injector and increasing with the blowing ratio. A generally good agreement is reached between numerical and experimental results at the different blowing ratios ($F = 0.045, 0.066, 0.11, 0.23$, corresponding to conditions B, C, D, E, respectively), with differences observed in the initial part of the curve, hence closer to the injector location, at the higher blowing ratios. The highest difference is seen for condition E at the initial position, 75 mm from the injector, due to the transitional flow, before convergence to similar values is obtained in the downstream region. An exception should be made for condition D, in which, after convergence is achieved between the experimental and numerical values at an intermediate position, the experimental curve reverses its trend

19

with a local increase in the effectiveness downstream of 92.5 mm. A plausible explanation of this might be the occurrence of a rapid transition process at the reported distance, caused by any potential source (e.g. an undetected roughness, or 3D/side effects) present at that particular experimental run (condition D), which then enhanced the mixing, hence the coolant concentration at the wall.
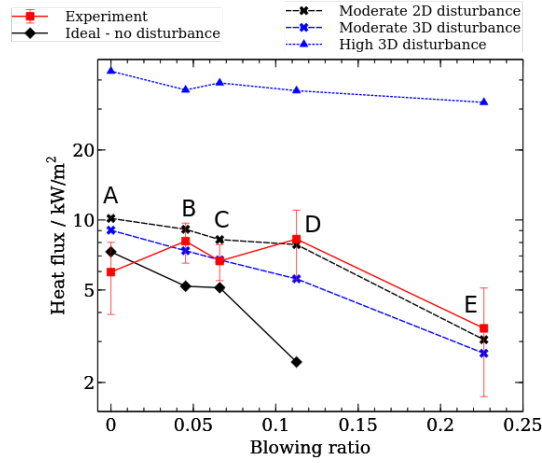

Figure 10: Wall heat flux at the different blowing ratios and for different disturbance amplitudes. Comparison between simulations and experiments
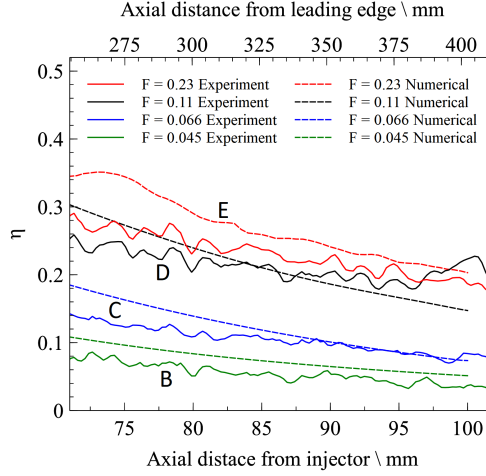
Axial distance from leading edge \ mm

Figure 11: Concentration based cooling effectiveness downstream of the slot injector. Comparison between simulations and experiments. The blowing ratios from F = 0.045 to F = 0.23 correspond to conditions from B to E respectively

7. Conclusion

DNS simulations have been run in conjunction with ground-test experiments to analyse the effects of boundary-layer instabilities and transition in a hypersonic flow on the wall cooling behaviour with slot injection. Dominant unstable modes pertaining to the class of first instabilities, found from an LST study, have been imposed inside the boundary layer with different amplitudes to simulate different states of the boundary layer, namely a perturbed laminar state for moderate amplitude forcing and a transitional state for high amplitude forcing, and to investigate their influence in different blowing ratio conditions.

Results indicate that transition induced by high-amplitude disturbances has a dramatic effect on the wall heat flux, while the presence of moderate amplitude unstable waves provides already a significant reduction of the beneficial effects of cooling, compared to an ideal case with no disturbances. Numerical results have been found to be consistent with the experimental measurements for both wall heat flux and cooling effectiveness for the moderate disturbance amplitude, indicating that the experimental condition corresponds to a perturbed condi-

21

tion preceding transition. The coolant distribution inside the boundary layer has been found to be significantly sensitive to the structure of the unstable mode evolution downstream. Moreover, significantly different mixing properties are observed dependent on transition being initiated by a high disturbance amplitude or a high blowing ratio, which has a strong impact on the cooling performance.

This study has shed light on the relation between boundary-layer unsteadiness due to instability modes and wall cooling performance, and is intended to serve as basis for future studies aimed at the correct design of efficient transpiration cooling systems and boundary-layer stabilisation for hypersonic vehicles.

Acknowledgments

References

[1] A. Fitt, J. Ockendon, T. Jones, Aerodynamics of slot-film cooling: theory and experiment, Journal of fluid mechanics 160 (1985) 15–27.

[2] A. Fitt, P. Wilmott, Slot film cooling—the effect of separation angle, Acta mechanica 103 (1-4) (1994) 79–88.

[3] S. Wittig, A. Schulz, M. Gritsch, K. A. Thole, Transonic film-cooling investigations: effects of hole shapes and orientations, in: ASME 1996 International Gas Turbine and Aeroengine Congress and Exhibition, American Society of Mechanical Engineers, 1996, pp. V004T09A026–V004T09A026.

[4] S. Baldauf, A. Schulz, S. Wittig, High-resolution measurements of local heat transfer coefficients from discrete hole film cooling, Transactions of the ASME-T-Journal of Turbomachinery 123 (4) (2001) 749–757.

[5] J. Meinert, J-ograve, r. Huhn, E. Serbest, O. J. Haidn, Turbulent boundary layers with foreign gas transpiration, Journal of Spacecraft and Rockets 38 (2) (2001) 191–198.

[6] T. Langener, J. V. Wolfersdorf, J. Steelant, Experimental investigations on transpiration cooling for scramjet applications using different coolants, AIAA journal 49 (7) (2011) 1409–1419.

[7] K. Heufer, H. Olivier, Experimental and numerical study of cooling gas injection in laminar supersonic flow, AIAA journal 46 (11) (2008) 2741–2751.

[8] M. A. Keller, M. J. Kloker, H. Olivier, Influence of cooling-gas properties on film-cooling effectiveness in supersonic flow, Journal of Spacecraft and Rockets 52 (5) (2015) 1443–1455.

[9] M. A. Keller, M. J. Kloker, Direct numerical simulation of foreign-gas film cooling in supersonic boundary-layer flow, Aiaa Journal 55 (1) (2016) 99–111.

[10] A. Fedorov, A. Shiplyuk, A. Maslov, E. Burov, N. Malmuth, Stabilization of a hypersonic boundary layer using an ultrasonically absorptive coating, Journal of Fluid Mechanics 479 (2003) 99–124.

[11] A. V. Fedorov, V. F. Kozlov, A. N. Shiplyuk, A. A. Maslov, N. D. Malmuth, Stability of hypersonic boundary layer on porous wall with regular microstructure, AIAA journal 44 (8) (2006) 1866–1871.

[12] L. M. Mack, Boundary-layer linear stability theory, Tech. rep., California Inst of Tech Pasadena Jet Propulsion Lab (1984).

[13] X. Wang, X. Zhong, The stabilization of a hypersonic boundary layer using local sections of porous coating, Physics of fluids 24 (3) (2012) 034105.

[14] V. Wartemann, H. Lüdeke, N. D. Sandham, Numerical investigation of hypersonic boundary-layer stabilization by porous surfaces, AIAA journal 50 (6) (2012) 1281–1290.

23

[15] N. Chokani, D. A. Bountin, A. N. Shiplyuk, A. A. Maslov, Nonlinear aspects of hypersonic boundary-layer stability on a porous surface, AIAA journal 43 (1) (2005) 149–155.

[16] S. Laurence, A. Wagner, K. Hannemann, Experimental study of second-mode instability growth and breakdown in a hypersonic boundary layer using high-speed schlieren visualization, Journal of Fluid Mechanics 797 (2016) 471–503.

[17] S. Lukashevich, S. Morozov, A. Shiplyuk, Experimental study of the effect of a passive porous coating on disturbances in a hypersonic boundary layer 2. effect of the porous coating location, Journal of Applied Mechanics and Technical Physics 57 (5) (2016) 873–878.

[18] A. Wagner, J. Martinez Schramm, C. Dittert, V. Sousa, D. I. Patel, C. Scalo, Experimental and numerical acoustic characterization of ultrasonically absorptive porous materials, in: 2018 Joint Thermophysics and Heat Transfer Conference, 2018, p. 2948.

[19] V. Sousa, D. I. Patel, J.-B. Chapelier, A. Wagner, C. Scalo, Numerical investigation of second mode attenuation over carbon/carbon surfaces on a sharp slender cone, in: 2018 AIAA Aerospace Sciences Meeting, 2018, p. 0350.

[20] S. P. Schneider, Effects of high-speed tunnel noise on laminar-turbulent transition, Journal of Spacecraft and Rockets 38 (3) (2001) 323–333. `arXiv:https://doi.org/10.2514/2.3705`, `doi:10.2514/2.3705`.
URL `https://doi.org/10.2514/2.3705`

[21] S. P. Schneider, Development of hypersonic quiet tunnels, Journal of Spacecraft and Rockets 45 (4) (2008) 641–664. `arXiv:https://doi.org/10.2514/1.34489`, `doi:10.2514/1.34489`.
URL `https://doi.org/10.2514/1.34489`

[22] S. P. Schneider, Developing mechanism-based methods for estimating hypersonic boundary-layer transition in flight: the role of quiet tunnels, in: 43rd AIAA Fluid Dynamics Conference, 2013, p. 2608.

[23] D. Masutti, E. Spinosa, O. Chazot, M. Carbonaro, Disturbance level characterization of a hypersonic blowdown facility, AIAA Journal 50 (12) (2012) 2720–2730. `doi:10.2514/1.j051502`.
URL `https://doi.org/10.2514/1.J051502`

[24] N. Parziale, J. Shepherd, H. Hornung, Free-stream density perturbations in a reflected-shock tunnel, Experiments in Fluids 55 (2) (2014) 1665.

[25] L. Duan, M. M. Choudhari, M. Wu, Numerical study of acoustic radiation due to a supersonic turbulent boundary layer, Journal of Fluid Mechanics 746 (2014) 165–192.

[26] A. Wagner, E. Schülein, R. Petervari, K. Hannemann, S. R. Ali, A. Cerminara, N. D. Sandham, Combined free-stream disturbance measurements and receptivity studies in hypersonic wind tunnels by means of a slender wedge probe and direct numerical simulation, Journal of Fluid Mechanics 842 (2018) 495–531.

[27] J. D. Anderson, Hypersonic and High-Temperature Gas Dynamics, Second Edition, AIAA Education Series, 2006.

[28] P. D. Neufeld, A. Janzen, R. Aziz, Empirical equations to calculate 16 of the transport collision integrals ω (l, s)* for the lennard-jones (12–6) potential, The Journal of Chemical Physics 57 (3) (1972) 1100–1102.

[29] D. J. Hill, D. I. Pullin, Hybrid tuned center-difference-weno method for large eddy simulations in the presence of strong shocks, Journal of Computational Physics 194 (2) (2004) 435–450.

[30] C. Pantano, R. Deiterding, D. J. Hill, D. I. Pullin, A low numerical dissipation patch-based adaptive mesh refinement method for large-eddy sim-

25

ulation of compressible flows, Journal of Computational Physics 221 (1) (2007) 63–87.

[31] J. L. Ziegler, R. Deiterding, J. E. Shepherd, D. I. Pullin, An adaptive high-order hybrid scheme for compressive, viscous flows with detailed chemistry, Journal of Computational Physics 230 (20) (2011) 7598–7630.

[32] M. Ihme, Y. Sun, R. Deiterding, Detailed simulations of weak-to-strong ignition of a h 2/o 2/ar mixture in shock-tubes, in: International Symposium on Shock Waves, Springer, 2013, pp. 209–214.

[33] A. Cerminara, R. Deiterding, N. Sandham, Dns of hypersonic flow over porous surfaces with a hybrid method, in: 2018 AIAA Aerospace Sciences Meeting, 2018, p. 0600.

[34] A. Cerminara, R. Deiterding, N. Sandham, Dns of hypersonic flow over porous surfaces with a hybrid method, in: 2018 AIAA Aerospace Sciences Meeting, 2018, p. 0600.

[35] R. Deiterding, Construction and application of an amr algorithm for distributed memory computers, in: Adaptive Mesh Refinement-Theory and Applications, Springer, 2005, pp. 361–372.

[36] A. Sansica, Stability and unsteadiness of transitional shock-wave/boundary-layer interactions in supersonic flows, Ph.D. thesis, University of Southampton (2015).

[37] M. Gaster, A note on the relation between temporally-increasing and spatially-increasing disturbances in hydrodynamic stability, Journal of Fluid Mechanics 14 (2) (1962) 222–224.

[38] M. McGilvray, L. J. Doherty, A. J. Neely, R. Pearce, P. Ireland, The oxford high density tunnel, in: 20th AIAA International Space Planes and Hypersonic Systems and Technologies Conference, no. 0 in International Space Planes and Hypersonic Systems and Technologies Conferences, American Institute of Aeronautics and Astronautics, 2015. `doi:`

10.2514/6.2015-3548.

475   URL https://doi.org/10.2514/6.2015-3548

[39] R. T. Penty Geraets, M. McGilvray, B. Williams, P. Shah, Laser-based calibration and processing technique for a robust fast-response surface heat transfer gauge, no. 0 in AIAA AVIATION Forum, American Institute of Aeronautics and Astronautics, 2018. doi:10.2514/6.2018-3772.

480   URL https://doi.org/10.2514/6.2018-3772

[40] M. L. G. Oldfield, Impulse response processing of transient heat transfer gauge signals, Journal of Turbomachinery, 2008, 130 (2). doi:10.1115/1.2752188.
URL https://doi.org/10.1115/1.2752188

485 [41] T. Hermann, H. S. Ifti, M. McGilvray, L. Doherty, R. P. Geraets, Mixing characteristics in a hypersonic flow around a transpiration cooled flat plate model, in: HiSST: International Conference on High-Speed Vehicle Science Technology, Moscow, Russia, 2018.

[42] A. Cerminara, R. Deiterding, N. Sandham, Parallel multiscale simula-
490   tion of hypersonic flow with porous wall injection, in: Proceedings of the Sixth International Conference on Parallel, Distributed, GPU and Cloud Computing for Engineering, Vol. 112, Civil-Comp Press, 2019, p. 18. doi:10.4203/ccp.112.11.
URL http://eprints.soton.ac.uk/id/eprint/431631

495 [43] M. H. Bashir, C.-C. Shiau, J.-C. Han, Film cooling effectiveness for three-row compound angle hole design on flat plate using psp technique, International Journal of Heat and Mass Transfer 115 (2017) 918–929.
URL   http://www.sciencedirect.com/science/article/pii/S0017931017300352

500   ‘